Transmission Lines Loaded with Pairs of Stepped Impedance Resonators: Modeling and Application to Differential Permittivity Measurements

Jordi Naqui, *Member*, *IEEE*, Christian Damm, *Member*, *IEEE*, Alex Wiens, *Student Member*, *IEEE,* Rolf Jakoby, *Member*, *IEEE*, Lijuan Su, *Student Member*, *IEEE*, Javier Mata-Contreras, and Ferran Martín, *Fellow, IEEE*

***Abstract*—Differential techniques are widely used in communication and sensor systems, as these techniques have been shown to improve the performance. This paper shows how differential sensing of permittivity can be conducted in a simple way. For that purpose, a microstrip line loaded with a pair of stepped impedance resonators is used in two different resonator connections: parallel and cascade. Each resonator is individually perturbed dielectrically so that: (*i*) when the two individual permittivities are identical, the structure exhibits a single resonance frequency; (*ii*) when the permittivies are different, resonance frequency splitting occurs, giving rise to two resonances (all these resonances are seen in the form of transmission zeros). The two sensing approaches are successfully validated through electromagnetic simulations and experiments. By virtue of a differential measurement, robustness against changing ambient factors that may produce sensor miscalibration is expected.**

***Index Terms*— differential measurement, dual-mode resonator, microstrip, microwave sensor, stepped-impedance resonator.**

I. Introduction

Permittivity sensors are prominent electromagnetic sensors whose development begun in the mid-twentieth century [1],[2]. These sensors are highly versatile, as the measurand (the physical quantity of interest) can be either the permittivity or another physical variable directly related to it.

This work was supported by MINECO-Spain (project TEC2013-40600-R), *Generalitat de Catalunya* (project 2014SGR-157), *Institució Catalana de Recerca i Estudis Avançats* (who awarded Ferran Martín), and by FEDER funds. Lijuan Su acknowledges the China Scholarship Council (CSC) for the grant 201306950011. This work was also partly supported by LOEWE STT.

J. Naqui, L. Su, J. Mata-Contreras and F. Martín are with GEMMA/CIMITEC, Departament d'Enginyeria Electrònica, Universitat Autònoma de Barcelona, 08193 Bellaterra, Spain (e-mail: Ferran.Martin@uab.es).

C. Damm, A. Wiens and R. Jakoby are with the Technische Universität Darmstadt, Merck str. 25, Darmstadt 64283, Germany.

C. Damm, A. Wiens, and R. Jakoby are with the Institute for Microwave Engineering and Photonics. Technische Universitaet Darmstadt (Merckstrasse 25) (64283 Darmstadt, Germany).

Nowadays, there are multiple technologies available to implement permittivity sensors. Nevertheless, the focus here is restricted to sensors consisting of passive planar transmission lines and/or resonators. In the last few years, many planar resonator-based permittivity sensors, where frequency shift is typically the electrical sensing variable, have been reported. These permittivity sensors are aimed at many topics, including material characterization [3]-[5] (this is indeed the context of the sensors proposed in this work), analysis of organic tissue [6][7], microfluidics [8]-[11], biosensing [12]-[16], or environmental factors [17]. Other planar permittivity sensors implemented by means of artificial transmission-lines have also been proposed [18]-[20].

A general drawback of resonance-based sensors is that, as permittivity depends on environmental conditions (e.g., temperature), the resonance frequency can be unintentionally shifted by spurious effects [2],[17]. As is well known, ideal sensors are designed to be linear or linear to some simple mathematical function with the measurand. However, sensors may be sensitive to other physical quantities, an effect designated as cross-sensitivity that entails measurement errors (miscalibration). Common cross-sensitivities are those derived from ambient factors; in sensor design, environmental stability is usually a key point and cannot be ignored [21],[22]. Regarding permittivity sensors, it can be argued that environmental drifts should be defined in terms of sensitivity rather than cross sensitivities. Nevertheless, if ambient factors are uncontrolled, the drifts should be indeed categorized into cross sensitivities. Additionally, the resonance frequency is generally dependent not only on the permittivity of interest, but also on the permittivity of the substrate/s necessary to support the resonant element [3]-[17]; this dependency is clearly a cross sensitivity.

In order to prevent or reduce systematic errors due to cross sensitivities as much as possible, several strategies can be utilized, such as compensation techniques, or the use of environmentally stable materials. Another typical solution to deal with changing environmental factors is through differential measurements, the one considered here. Differential measurements are robust against variable ambient

conditions provided that these conditions perturb in the form of a common-mode stimulus. Generally, two sensors are used to construct a differential sensor, both of them being subjected to the same external factors [18]-[22]; an ideal sensor should be capable of conducting measurements regardless of the surrounding ambient factors.

Depending on the application, differential measurements can be used with sensing or comparison purposes. A differential sensor measures the difference in permittivity (or one of the two permittivities, provided that the other one is known), whereas a comparator (differential by definition) can be used to inquire about whether two permittivities are the same or not. Permittivity comparators may be of interest, for instance, for the detection of defects or alteration of a SUT (sample under test) by comparing it to a well-known reference.

A differential permittivity sensor based on amplitude levels by means of an interferometer setup was reported in [18]-[20]. In [23] the authors presented a differential sensor/comparator consisting of a transmission line loaded with a pair of identical shunt-connected stepped-impedance resonators (SIRs) connected to the same junction. Instead of duplicating and combining sensors in pairs to construct a differential sensor, pairs of resonators connected to a single signal interface (a single transmission line) were employed. Because of the SIR semi-lumped behavior, the size was compact, and electric energy was concentrated in a small region allowing for small SUTs and for low cross sensitivities (if present) related to substrate/s. Due to the SIR high Q-factor, high frequency discrimination was expected. The sensing principle, experimentally validated in the vicinity of 60 GHz, is based on resonance frequency splitting derived from symmetry perturbation [23]-[25]; there is one or two transmission zeros depending on whether the two permittivities are the same or not, respectively. However, the inter-resonator coupling was seen to degrade considerably the sensitivity and discrimination for small differential inputs.

This work is aimed at expanding the preliminary research work conducted in [23], with a view to performing real-time differential permittivity measurements. Further analysis for the topology proposed in [23] is carried out, and an alternative topology based on a transmission line loaded with a cascade connection of SIRs to face with the drawback of the original topology is proposed. Equivalent circuit models are proposed and validated, from which the theoretical sensitivity is inferred. Experimental data applying material permittivity perturbation is reported to validate the potentiality of the proposed approaches. As will be proven, the new proposed structure exhibits significant benefits against the original one when the individual permittivities attain close values; higher sensitivity, higher discrimination, and narrower bandwidth of operation.

This paper is organized as follows. Section II is devoted to show the two considered physical sensing topologies, and to their modeling by equivalent circuits. In Section III, the capabilities of these structures to operate as a differential sensor or a comparator are investigated by analyzing the sensitivity and the discrimination, respectively. Next, Section IV reports experimental verifications of the sensing approaches. Finally, the main conclusions are drawn in Section V.

II. Topologies and Equivalent Circuit Models

This section analyzes transmission lines loaded with a pair of shunt-connected stepped impedance resonators (SIRs) in two different topologies; one with the SIRs loaded at the same junction, and the other one by cascading the SIRs. Two SIRs are used to perform a real-time (i.e., through a single measurement) differential measurement. Furthermore, the two SIRs are identical with the purpose of rejecting as much as possible common-mode stimulus. Equivalent circuit models including independent and arbitrary capacitive variations in the SIRs are presented and validated. Without loss of generality, we use microstrip implementation. Losses are disregarded throughout this work, eligible approximation when dealing with low-loss substrates and SUTs. Nevertheless, a method to estimate the loss factor is included in the last section.

A. Microstrip Line Loaded with a pair of parallel SIRs

The SIR in Fig. 1(a), in shunt connection to a microstrip line section, is a semi-lumped resonator [26]. Provided that the two sections are electrically small, the behavior of a shunt-connected SIR may be approximated to that of a shunt-connected lumped LC resonator. The inductance/capacitance of the SIR is essentially determined by the inductance/capacitance of the high/low impedance section. Consequently, the circuit model depicted in Fig. 1(b) may describe accurately a microstrip line loaded with a single SIR. The inductance and capacitance of the main host transmission line are L and C, respectively, whereas the SIR inductance and capacitance are L_s and C_s, respectively. Additionally, for sensing purposes, the model takes into account a capacitive perturbation, ΔC_s, applied to the SIR. According to the circuit model of Fig. 1(b), a transmission zero (or notch) appears at the angular resonance frequency given by

$$\omega_0 = \frac{1}{\sqrt{L_s\left(C_s \pm |\Delta C_s|\right)}}. \tag{1}$$

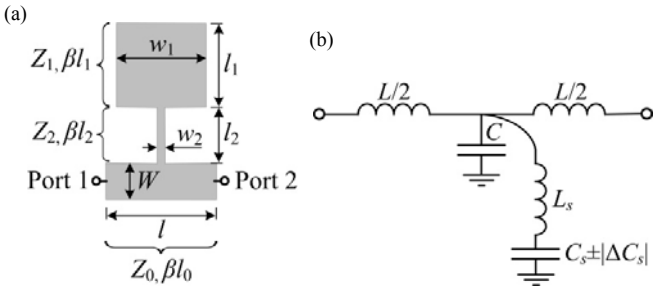

Fig. 1. (a) Typical topology of a SIR-loaded microstrip line, where geometrical and electrical parameters are indicated. (b) Equivalent circuit model with a capacitive perturbation applied to the SIR.

As a case study a single SIR-loaded line with dimensions $W = 1.83$ mm, $l = 6$ mm, $l_1 = l_2 = 2.6$ mm, $w_1 = 5.5$ mm, and $w_2 = 250$ μm and substrate *Rogers RO4003C* with relative permittivity $\varepsilon_r = 3.38$, thickness $h = 812.8$ μm, and loss tangent $\tan\delta = 0.0021$, was considered in [23]. The model was validated by circuit simulation of extracted parameters, inferred following the systematic procedure reported in [27], which is based on a mapping of the scattering parameters obtained from full-wave electromagnetic simulation, adapted to the considered circuit. The resulting circuit parameters, characteristic impedances and electrical lengths were found to be: $Z_0 = 50$ Ω, $Z_1 = 23$ Ω, and $Z_2 = 120$ Ω, electrical lengths at $f_0 = 3.83$ GHz were $\beta l_0 = 45°$, $\beta l_1 = 21°$, and $\beta l_2 = 18°$, and the circuit elements were $L = 1.81$ nH, $C = 0.57$ pF, $L_s = 2.45$ nH, and $C_s = 0.70$ pF ($\Delta C_s = 0$).

In order to verify the modeling of an alteration in the resonator capacitance, a shape perturbation was produced in [23]. Namely, the length of the wide section of the reference resonator was enlarged ($+|\Delta l_1|$) or shortened ($-|\Delta l_1|$), with $\Delta l_1 = \pm 0.5$ mm $= \pm 0.19 l_1$, to increase ($+|\Delta C_s|$) or decrease ($-|\Delta C_s|$) its associated capacitance, respectively. The circuit values of these perturbations ($\pm|\Delta C_s|$), with $\Delta C_s = \pm 0.11$ pF $= \pm 0.15 C_s$, were obtained from (1) and the transmission zero frequencies inferred from electromagnetic simulations. The transmission coefficient of these structures, confirmed that the circuit simulations were in good accordance with those inferred from electromagnetic solvers in [23].

As expected from (1), any capacitive perturbation may be sensed by monitoring the change in the resonance frequency. However, a real-time differential measurement of two capacitive perturbations cannot be performed by loading a transmission line with a single SIR. Therefore, transmission lines loaded with pairs of SIRs are necessary.

Fig. 2(a) shows a microstrip line loaded with a pair of identical shunt-connected SIRs placed at the same junction, and on opposite sides of the line (parallel configuration). In this topology, as was already considered in [23], it is assumed that both resonators are individually and simultaneously capacitively-perturbed by ΔC_{si} ($i = 1, 2$). The lumped element equivalent circuit model that was proposed in [23] is represented in Fig. 2(b). The SIRs are close together, and magnetic coupling between them is accounted for, such a coupling being negative since the currents in the mirrored SIRs flow in opposite directions (i.e., the currents are anti-parallel at the junction of the SIRs). This coupling is accounted for by the mutual inductance $-|M|$, the magnetic coupling coefficient being [26]

$$k_m = -\frac{|M|}{L_s}. \tag{2}$$

From the equivalent T-circuit model of a two-port network consisting of a pair of coupled inductors, the circuit model shown in Fig. 2(c) is inferred. If the capacitive perturbations are identical ($\Delta C_{s1} = \Delta C_{s2} = \Delta C_s$), the simpler circuit depicted in Fig. 2(d) results.

For balanced (i.e., identical) perturbations, according to the circuit of Fig. 2(d), it can be readily noticed that the structure exhibits a single transmission zero at

$$\omega_e = \frac{1}{\sqrt{\left(L_s - |M|\right)\left(C_s \pm |\Delta C_s|\right)}} = \frac{\omega_0}{\sqrt{1 - |k_m|}}. \tag{3}$$

In the presence of coupling, the transmission zero simply shifts upwards. The resonance frequency in (3) is denoted by ω_e, in agreement to the nomenclature used in [26] to emphasize the presence of an open circuit, under even mode excitation, at the symmetry plane of two identical coupled resonators.

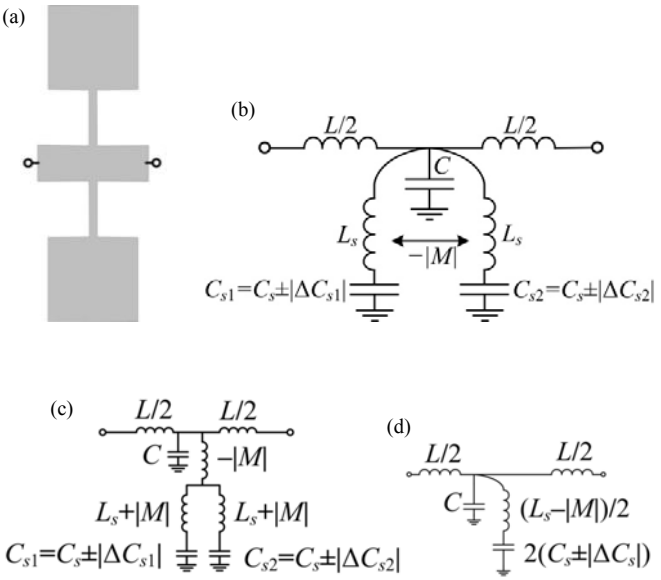

Fig. 2. (a) Microstrip line loaded with a pair of identical SIRs at the same junction and on opposite sides. (b) Equivalent circuit model with arbitrary capacitive perturbations in the two SIRs. (c) Transformed equivalent circuit model. (d) Transformed and simplified equivalent circuit model with balanced perturbations.

In the case with different perturbations ($\Delta C_{s1} \neq \Delta C_{s2}$), the symmetry in the shunt branch of the circuit model is disrupted. Although the resulting circuit model is not as simple as with balanced perturbations, the resonance condition can be easily obtained by setting the shunt branch impedance to zero. This gives the resonance frequencies of a circuit network composed of two magnetically coupled resonators, given by [26]

$$\omega_{l,u} = \sqrt{\frac{L_s\left(C_{s1} + C_{s2}\right) \pm \sqrt{\left[L_s\left(C_{s1} - C_{s2}\right)\right]^2 + 4C_{s1}C_{s2}M^2}}{2C_{s1}C_{s2}\left(L_s^2 - M^2\right)}}, \tag{4}$$

where ω_l and ω_u denote the lower and upper resonance frequencies, respectively. Therefore, a jump discontinuity arises due to unbalanced perturbations giving rise to two split resonance frequencies. The most relevant aspect is the fact that, because of coupling, the two resonances depend on the two perturbations, i.e., $\omega_{l,u} = f(\Delta C_{s1}, \Delta C_{s2})$. Accordingly, each resonance frequency cannot be independently tuned by its corresponding perturbation. In other words, when one of the resonators is perturbed, the two resonance frequencies change

(the more similar the perturbations, the higher the cross-dependence). It turns out that a parallel combination of shunt-connected SIRs can be viewed as a dual-mode tri-section (wide-narrow-wide) SIR [28]-[32], where symmetry disruption is necessary to invoke the dual-mode behavior [33]. Note that multimode resonators are usually utilized to reduce the size of circuits, but in the present work a dual resonant behavior is used to conduct a differential measurement.

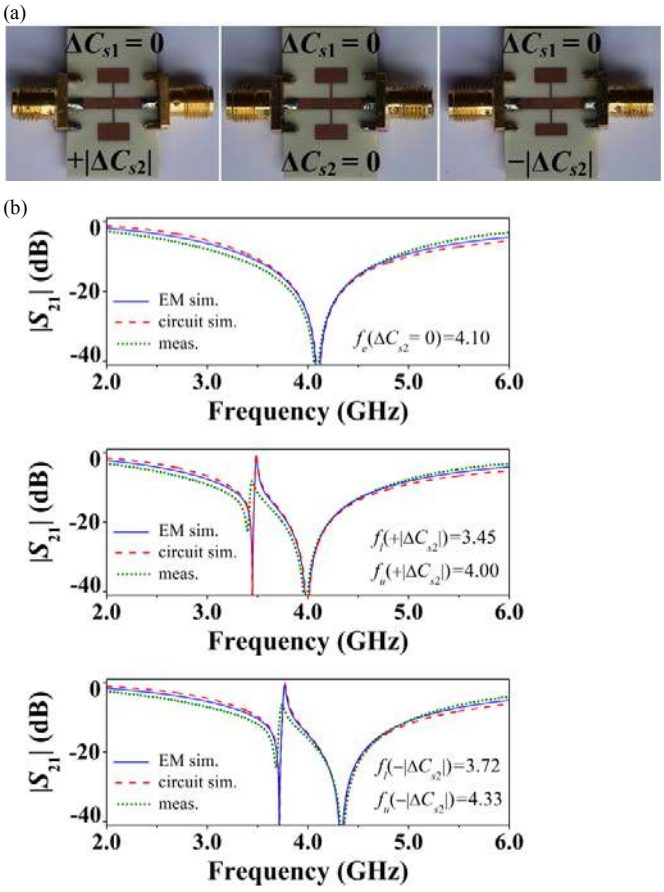

Fig. 3. (a) Photograph of the considered microstrip lines loaded with pairs of parallel SIRs. The lower SIR is perturbed by $\pm|\Delta C_{s2}|$, whereas the upper SIR is unperturbed ($\Delta C_{s1} = 0$). The dimensions and substrate are those indicated in the text in reference to the single SIR-loaded line of [23] (except $l = 15.9$ mm to solder the connectors). (b) Magnitude of the transmission coefficient obtained from lossless electromagnetic and circuit simulations, and measurements. The circuit parameters are those indicated in the text for the single SIR-loaded line of [23], with $M = -0.31$ nH ($k_m = -0.13$), as the additional host line length produces a phase shift only. The indicated resonance frequencies correspond to those obtained by simulation.

In order to demonstrate the validity and usefulness of the models in Fig. 2, in [23] three different pairs of SIRs loading a microstrip line were considered, as can be seen in Fig. 3(a): a symmetric pair, an asymmetric pair derived by increasing l_1 in one of the SIRs ($+|\Delta C_{s2}|$), and another asymmetric pair derived by decreasing l_1 ($-|\Delta C_{s2}|$). These structures were already fabricated (using a drilling machine) and measured in [23], but some fabrication-related tolerances and uncertainties were observed. For this reason, we have fabricated them again (using a photo-etching process) to fit better the measurements with the simulations. As the considered structures are built up from those of single SIR loaded line, the only circuit parameter that needs to be obtained is the mutual inductance. This parameter has been obtained by curve fitting the circuit simulation to the electromagnetic simulation in the case of the host line loaded with symmetric SIRs. Analytically, (3) can be used alternatively. The extracted value is $M = -0.31$ nH ($k_m = -0.13$). As proven in Fig. 3(b), the circuit simulations are consistent with both electromagnetic simulations and measurements, verifying that losses omission is a reasonable approximation using low-loss substrates.

It should be noted from Fig. 3 that the resonance frequency at f_u resembles that at f_e, while an additional narrowband lower resonance frequency at f_l appears. When symmetry (in regard to the line axis) is broken, the bandwidth at f_l is narrower than that at f_u. The smaller the difference in the perturbations, the narrower the lower notch. As a result, the discrimination to detect small differences between the perturbations is expected to be degraded by losses.

B. Microstrip Line Loaded with a Pair of Cascaded SIRs

This subsection deals with an alternative topology presented in this paper to perform differential capacitive measurements in such a way that inter-resonator coupling is prevented. The proposed topology is illustrated in Fig. 4(a), and consists of a transmission line loaded with a cascade connection of two identical SIRs which are spaced apart by a transmission line section of length l_s. If the SIRs are loaded on the same side of the line, as is considered, the resonators may be coupled not only magnetically, but also electrically. However, the resonators are placed sufficiently separated so that we may assume that the total coupling is negligible.

The proposed circuit model is that represented in Fig. 4(b). Regardless of the length of the transmission line section between resonators, l_s, the transmission zero frequencies are given by

$$\omega_l = \min\left(\frac{1}{\sqrt{L_s\left(C_s \pm |\Delta C_{s1}|\right)}}, \frac{1}{\sqrt{L_s\left(C_s \pm |\Delta C_{s2}|\right)}}\right), \quad (5a)$$

$$\omega_u = \max\left(\frac{1}{\sqrt{L_s\left(C_s \pm |\Delta C_{s1}|\right)}}, \frac{1}{\sqrt{L_s\left(C_s \pm |\Delta C_{s2}|\right)}}\right), \quad (5b)$$

where ω_l and ω_u denote again the lower and upper resonance frequencies, respectively. According to the previous expressions, the two resonances can be shifted independently like using single SIRs, even for unbalanced perturbations. Clearly, the resonance frequency splitting phenomenon, which emerges from unbalanced perturbations, is of different nature in the two configurations under study. In cascaded SIRs, splitting occurs as a mere result of frequency shifting, whereas in parallel SIR there is a combination of frequency shifting and inter-resonator coupling.

Let us now assume the particular case where the in-between transmission line section is half-wavelength long ($l_s = \lambda/2$, where λ is the guided wavelength). As the input impedance of a load seen through a $\lambda/2$ line is unchanged, the circuit in Fig.

4(b) is equivalent to that shown in Fig. 4(c). Note that the SIRs are virtually connected at the same junction so that the structure behaves like if the SIRs were physically located at the same junction (due to periodicity, this holds at integer multiples of $\lambda/2$). Indeed, the latter circuit is the ideal one which we would like to implement. The problems to implement this idealized circuit are: (*i*) in parallel SIRs, there is inter-resonator coupling (Section II-B); (*ii*) in cascaded SIRs, $l_s = \lambda/2$ is satisfied at one frequency only (this condition is designed to be satisfied at the resonance frequency of the unperturbed resonators). However, the latter issue is not dramatic, since the resonance frequencies in (5) do not depend on the inter-resonator distance (as long as inter-resonator coupling can be ignored). Therefore, the resonance frequencies of the model in Fig. 4(c) always coincide with those of the model in Fig. 4(b).

The last simplification makes the assumption that the perturbations are identical ($\omega_l = \omega_u = \omega_0$). In this circumstance, the circuit in Fig. 4(c) derives to the one in Fig. 4(d), which is formally identical to that with parallel SIRs depicted in Fig. 2(d).

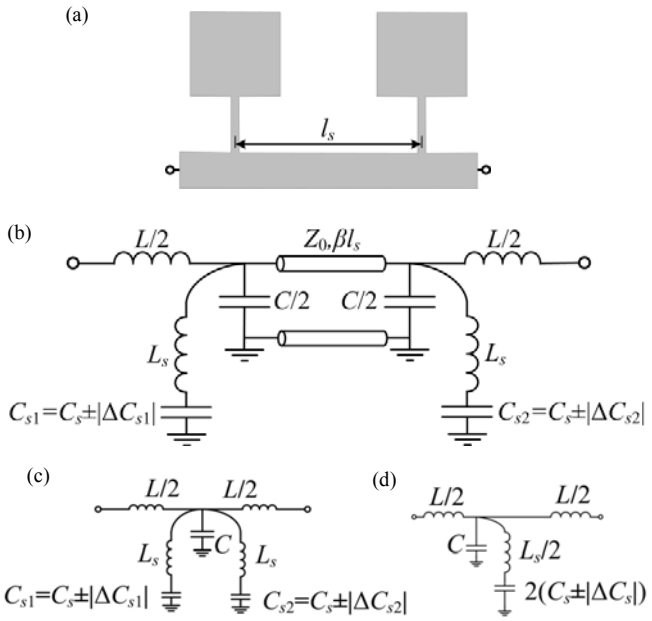

Fig. 4. (a) Microstrip line loaded with a pair of identical SIRs in cascade connection. (b) Equivalent hybrid circuit/TL model including arbitrary capacitive perturbations. (c) Simplified equivalent circuit model when the resonators are spaced half-wavelength apart, i.e., the in-between transmission line section has an electrical length of $\beta l_s = 180°$. (d) Simplified equivalent circuit model for $\beta l_s = 180°$ in the case of balanced perturbations.

To demonstrate the usefulness of the cascaded approach, we have considered the same three previous scenarios in line with the parallel connection [see Fig. 5(a)]. Accordingly, the same circuit elements have been used to validate the equivalent circuit models. As can be seen in Fig. 5(b), the agreement between the circuit/TL simulations, the electromagnetic simulations, and measurements is quite good. It deserves mentioning that a small ripple can be noticed from measurements in the symmetric structure, owing to the fact that the in-between transmission line is not exactly half-wavelength at the corresponding resonance frequency. Importantly, the notch frequencies are the same as those using single SIRs. Another relevant result is that the bandwidth of both notches is not narrow by nature, in contrast to what occurs at the lower resonance frequency employing parallel SIRs.

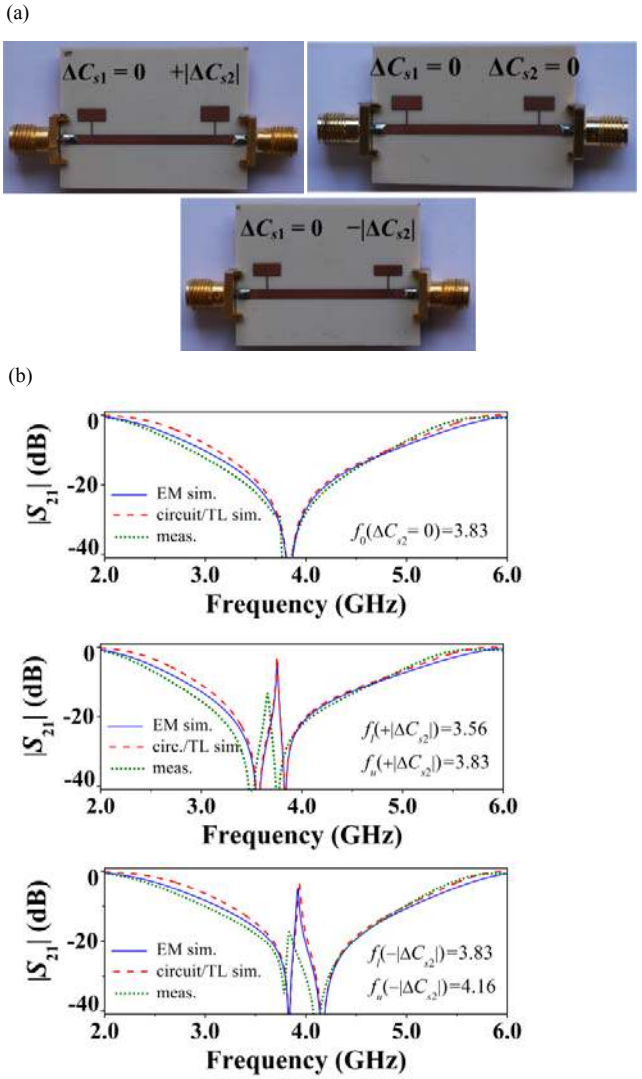

Fig. 5. (a) Photograph of the considered microstrip lines loaded with pairs of cascaded SIRs. The right SIR is perturbed by $\pm|\Delta C_{s2}|$, whereas the left SIR is unperturbed ($\Delta C_{s1} = 0$). The dimensions, substrate, and circuit parameters are those of the single SIR-loaded line (except $l_s = 23.9$ mm and $l = 35.9$ mm). (b) Transmission coefficient magnitude obtained from lossless electromagnetic and circuit/TL simulations, and measurements. The indicated resonance frequencies correspond to simulations.

C. *Comparison between the Topologies*

To end this section, we compare the transmission zero frequencies given by the two considered configurations, namely, those depicted in Figs. 3(a) and 5(a).

The results for the three considered scenarios with different perturbations [Figs. 3(b) and 5(b), as well as the single SIR] are plotted in Fig. 6 for comparison purposes. In the light of this figure, it is clear that the two concerning topologies manifest a strongly different behavior caused by the presence or absence of inter-resonator coupling.

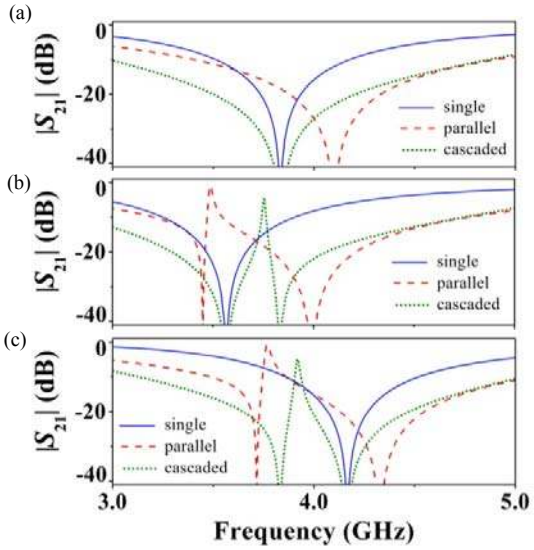

Fig.6. Transmission coefficient magnitude (lossless electromagnetic simulation) of the considered microstrip lines loaded with parallel or cascaded SIRs for $\Delta C_{s1} = 0$, and (a) $\Delta C_{s2} = 0$, (b) $+|\Delta C_{s2}|$, and (c) $-|\Delta C_{s2}|$. For comparison purposes, the response using a single SIR [23] applying to it ΔC_{s2} is also plotted.

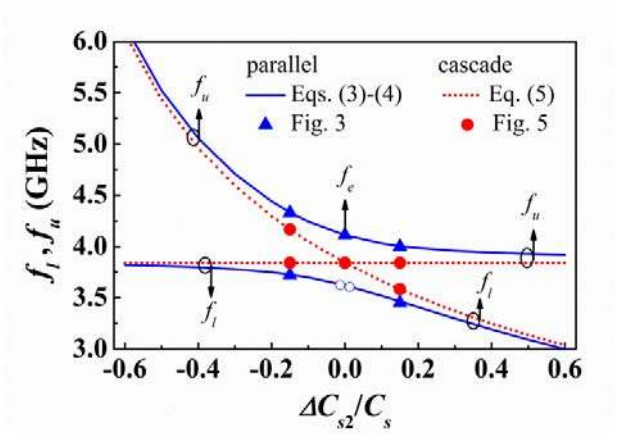

Fig. 7. Resonance frequencies predicted by (3)−(4) and (5) versus a capacitive perturbation ($\Delta C_{s1} = 0$ and $-0.6 \le \Delta C_{s2} / C_s \le 0.6$) for the considered reference microstrip lines loaded with parallel and cascaded SIRs, respectively. The circuit parameters of the reference structures are: $L = 1.81$ nH, $C = 0.57$ pF, $L_s = 2.45$ nH, $C_s = 0.70$ pF, and $M = -0.31$ nH. The resonance frequencies of the three basic scenarios of Figs. 3 and 5, which correspond to particular perturbations, are mapped.

Fig. 7 plots the resonance frequencies predicted by (3)−(4) and (5) in the case where a capacitive perturbation is applied to one of the SIRs ($\Delta C_{s1} = 0$ and $\Delta C_{s2} \neq 0$). The considered circuit parameters of the unperturbed structures are those obtained previously. Additionally, the resonances for the particular perturbed structures are also mapped to the curves. It is especially visible that, when one of the resonators is perturbed ($\Delta C_{s2} \neq 0$), the frequency splitting in parallel SIRs is characterized by a shift in the two resonances. On the contrary, for cascaded SIRs only the resonance frequency of the perturbed resonator is shifted.

In conclusion, it can be drawn that a cascade connection of SIRs provides a good solution to prevent coupling between them. Moreover, significant advantages arise, particularly, the resonances are independent to each other (enhancing the sensitivity, as will be shown in Subsection III-C), their bandwidth is moderately wide by nature (improving the discrimination), the spectral separation between the resonance frequencies is not enhanced by coupling (requiring a narrower bandwidth of operation), and unknown perturbations can be physically identified. As will be shown, these advantages hold as long as the perturbations are similar.

III. Sensitivity Analysis

Thus far, capacitive perturbations have been produced by changing the physical dimensions of the resonators. Evidently, in practice, the capacitive perturbations in a permittivity sensor must be due to permittivity perturbations of samples under test (SUTs). We use the term *sample* in order not to lose generality, meaning that the sample can be a material, liquid, organic tissue, and so forth. Furthermore, the SUT may also refer to a functional layer that enhances the measurand-to-permittivity relationship for sensing purposes (e.g., in environmental sensors based on functional layers, a material highly sensitive to the environmental factor of interest is used).

This section evaluates the sensitivity in differential permittivity measurements, for both capacitive and permittivity perturbations. The study is conducted on the basis of the proposed equivalent circuit models, together with analytical expressions of capacitances, and on electromagnetic simulations.

A. Analytical Sensitivity in terms of Capacitance

With a view to performing differential sensing of capacitances in the considered approach based on frequency splitting, the differential input is the difference between the capacitances, that is

$$C_{sd} = C_{s2} - C_{s1}. \tag{6}$$

The output electrical variable to be monitored is frequency, and the differential output is defined as the difference between the upper and lower resonance frequencies, that is

$$f_d = f_u - f_l. \tag{7}$$

Obviously, despite the fact that the resonance for balanced perturbations is denoted by f_e or f_0, when a single resonance is monitored, implicitly results $f_l = f_u$. The curve that relates the output and input quantities, namely $f_d(C_{sd})$, is named transfer function, whose slope is the sensitivity. Hence, the sensitivity is defined as the variation in the difference between the resonance frequencies divided by the variation in the difference between the capacitances. Mathematically, the sensitivity can be written as

$$S = \frac{df_d}{dC_{sd}} = \lim_{\Delta C_{s2} - \Delta C_{s1} \to 0} \frac{\Delta f_u - \Delta f_l}{\Delta C_{s2} - \Delta C_{s1}}, \quad (8)$$

where ΔC_{si} ($i = 1, 2$) and $\Delta f_{l,u}$ stand for individual incremental/decremental changes in capacitance and resonance frequency, respectively. For simplicity, if one of the SIRs is not perturbed and considered to be a reference (so that $\Delta C_{s1} = 0$) then (8) reduces to

$$S = \frac{df_d}{dC_{s2}} = \lim_{\Delta C_{s2} \to 0} \frac{\Delta(f_u - f_l)}{\Delta C_{s2}}. \quad (9)$$

In addition, in the cascade configuration, the magnitude of the analytical sensitivity for null perturbation (y-axis) becomes

$$|S| = \frac{f_0}{2C_{s2}}. \quad (10)$$

The sensitivity should be as high as possible, and constant values of it are preferred. In order to gain insight into the sensitivity, instead of analyzing (9), that is cumbersome when the resonance frequencies are governed by (4), numerical solutions will be given. The resonance frequencies determined by (3)−(4) for two different coupling coefficients and by (5) are plotted in Fig. 8(a) assuming $\Delta C_{s1} = 0$. It is evident that the output is null in the case of a perfect balance of perturbations ($\Delta C_{s1} = \Delta C_{s2} = 0$). On the other hand, unbalanced perturbations have been introduced by a capacitive variation in one of the SIRs ($\Delta C_{s1} = 0$, $\Delta C_{s2} \neq 0$). As expected, when $k_m \neq 0$, corresponding to the case with parallel SIRs, f_u is more sensitive to $-|\Delta C_{s2}|$ than f_l, and complementarily f_l is more sensitive to $+|\Delta C_{s2}|$. Both frequencies tend to the frequencies without coupling as the capacitive perturbation increases.

Fig. 8(b) shows the corresponding transfer function from which it is apparent that, as $|k_m|$ increases, the frequency splitting, f_d, strengthens. It turns out that the sensitivity, shown in Fig. 8(c), worsens as $|k_m|$ increases. Indeed, the maximum sensitivity corresponds to the case of (uncoupled) cascaded SIRs, and is given by (10). Specifically, a significant degradation in the sensitivity results for small perturbations. As was stressed earlier, even for loose coupling coefficients, coupling cannot be neglected for similar perturbations. Nevertheless, the parallel configuration can be useful when the perturbations differ from each other significantly. In these situations, coupling plays an insignificant role.

The results in Fig. 8 were already published in [23], where using parallel SIRs with $k_m = 0$ was assumed to be fictitious. Here, $k_m = 0$ is no longer fictitious, as is implemented employing cascaded SIRs. For small inputs, since the inter-resonator coupling in parallel SIRs decreases the sensitivity, parallel-connected SIRs are apparently not much appropriate to properly operate as a sensor. Additionally, this topology working as a comparator between two capacitively-perturbed SIRs is not much promising. As mentioned before, the discrimination for small differential inputs is expected to be rather limited due to the narrowband nature of the lower resonance. Conversely, SIRs in cascade connection are expected to achieve high sensitivities and discriminations.

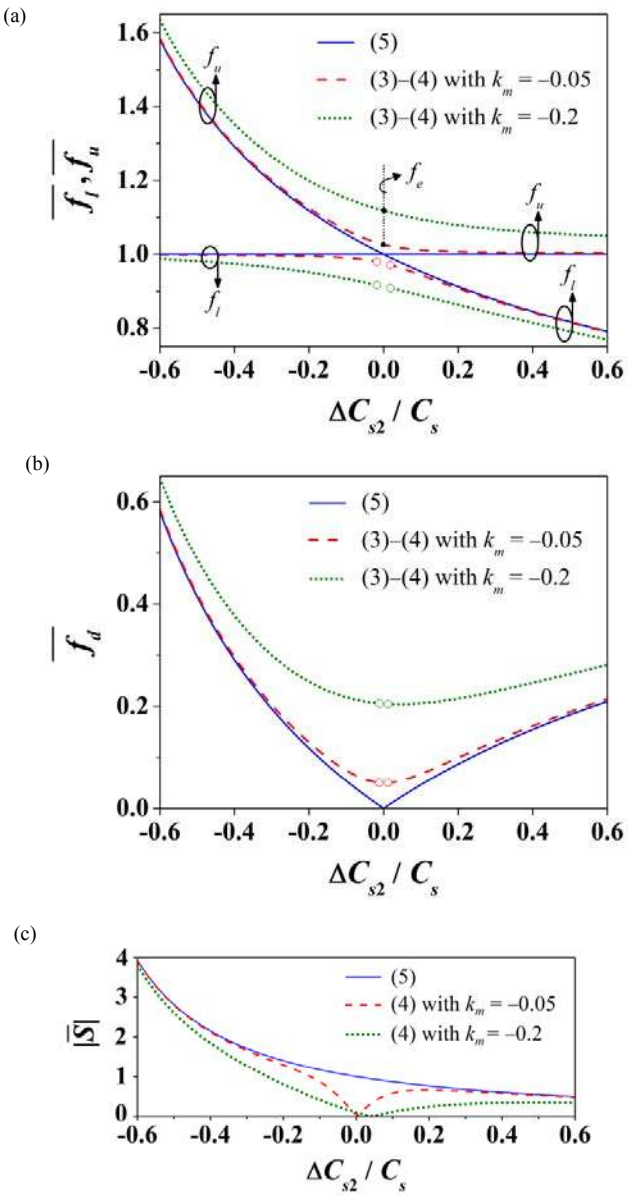

Fig. 8. (a) Resonance frequencies given by (3)−(4) for different k_m and (5) normalized to the constant resonance frequency of the non-perturbed uncoupled SIR determined by (5). The capacitive perturbations are $\Delta C_{s1} = 0$ and $-0.6 \leq \Delta C_{s2} / C_s \leq 0.6$. (b) Normalized transfer function. (c) Sensitivity magnitude normalized to the case of balanced perturbations ($\Delta C_{s2} = 0$) in the cascaded configuration. For the parallel arrangement, sensitivity is calculated using (4) solely, disregarding (3) in order not to calculate the sensitivity across the jump discontinuity.

It should be mentioned that the dynamic range of measurement is not limited to the considered one ($|\Delta C_{s2}| \leq 0.6 C_s$). This relatively small dynamic range, however, allows for illustrating properly the handicap of the parallel configuration, i.e., low performance under small inputs. Finally, it is also important to highlight that the sensitivity is not constant due to the fact that the transfer function is not linear [this is indeed evident from the simplest form of the sensitivity given by (10)]. Moreover, sensitivity is

not a symmetric function with respect to the *y*-axis, i.e., $S(+|\Delta C_{sd}|) \neq S(-|\Delta C_{sd}|)$. Instead, the sensitivity magnitude increases or decreases as the input capacitance is increasingly lower or higher, respectively.

B. Analytical Sensitivity in terms of Permittivity

In the previous subsection we considered a capacitive input as a generalization. Capacitive variations can be produced by several means, e.g., by changing the physical dimensions of the resonators (i.e., shape perturbation as done in Section II) or by changing dielectric properties (i.e., material perturbation, as it must be in practice). Therefore, in a real sensor the differential input is the difference in the relative permittivity of the SUTs, defined here as

$$\varepsilon_{rd} = \varepsilon_{r2} - \varepsilon_{r1}. \tag{11}$$

It should be noted that the sensor measures a difference between two permittivities. Provided that one of the two permittivites is known, the other permittivity can be inferred.

The sensitivity in terms of the relative permittivity becomes

$$S = \frac{\partial f_d}{\partial \varepsilon_{rd}} = \lim_{\Delta\varepsilon_{r2}-\Delta\varepsilon_{r1}\to 0} \frac{\Delta f_u - \Delta f_l}{\Delta\varepsilon_{r2} - \Delta\varepsilon_{r1}}, \tag{12}$$

where $\Delta\varepsilon_{ri}$ (i = 1, 2) stands for changes in relative permittivity. The partial derivatives indicate that the output differential frequency may be influenced by other physical variables related to cross sensitivities, as will be illustrated before ending this subsection. By assuming a linear dependence of the capacitance with the permittivity (with proportionality constant k), and letting $\Delta\varepsilon_{r1} = 0$ and $k_m = 0$ once again, the sensitivity magnitude becomes

$$|S| = \frac{f_0}{2\varepsilon_{r2}}. \tag{13}$$

To establish analytically the transfer function and sensitivity above, the SIR capacitance was approximated by the parallel-plate capacitance of its wide section, namely

$$C_p = \frac{\varepsilon_0 \varepsilon_{r2} w_1 l_1}{h} = k\varepsilon_{r2}, \tag{14}$$

where ε_0 is the vacuum permittivity. In (14), the substrate in the vicinity of the wide section is supposed to be replaced with one SUT. The most relevant aspect in this approximation is that the SIR capacitance is linearly dependent on the permittivity. The corresponding capacitance for the reference SIR is C_p = 0.53 pF. However, (14) must be considered as a first-order approximation as mentioned above, where $l_1, w_1 >> h$ are required for accurate results. Likewise, C_s is neither exactly proportional to l_1; $\Delta l_1 = \pm 0.19 l_1$ produces $\Delta C_s = \pm 0.15 C_s$.

Finally, to illustrate the robustness of differential measurements against cross sensitivities, let us assume that we compare two identical materials ($\Delta C_s = \Delta C_{s1} = \Delta C_{s2}$). Using a two-step process with a single SIR, the resulting resonance frequencies are

$$\omega_0 = \frac{1}{\sqrt{L_s\left(C_s + \Delta C_s\right)}}. \tag{15}$$

Let us now introduce a spurious change in the capacitance related to a cross sensitivity, denoted by ΔC_{xi} (i = 1,2). As the effect of cross sensitivities may change over time, one may assume $\Delta C_{x1} \neq \Delta C_{x2}$ (neither a compensation technique nor recalibration is considered). Hence, in the presence of cross sensitivities, the different drifts shift the resonance frequencies to

$$\omega_{01} = \frac{1}{\sqrt{L_s\left(C_s + \Delta C_s + \Delta C_{x1}\right)}}, \tag{16a}$$

$$\omega_{02} = \frac{1}{\sqrt{L_s\left(C_s + \Delta C_s + \Delta C_{x2}\right)}}. \tag{16b}$$

Therefore, $f_d \neq 0$ and the readout is going to be wrong. By contrast, performing the proposed real-time differential measurement, using the cascaded configuration, the resulting single resonance frequency is

$$\omega_l = \omega_u = \omega_0 = \frac{1}{\sqrt{L_s\left(C_s + \Delta C_s\right)}}. \tag{17}$$

Since the two materials are the same and affected by cross sensitivities at the same time, it is reasonable to assume that $\Delta C_x = \Delta C_{x1} = \Delta C_{x2}$, so that

$$\omega_l = \omega_u = \omega_0 = \frac{1}{\sqrt{L_s\left(C_s + \Delta C_s + \Delta C_x\right)}}. \tag{18}$$

Consequently, $f_d = 0$, indicating that there is no difference between the materials. Note, however, that a comparison between identical materials is the most favorable case to reject cross sensitivities, this case being theoretically totally immune to them, as indicated by (18). In a differential sensing, some degree of robustness is expected, as different materials may respond in a different way to the same stimulus. Particularly, if we compare f_d for different materials (characterized by $\Delta C_{s1} = 0$, $\Delta C_{s2} = \Delta C_s$), and the same quantity under the presence of a common mode stimulus f_d', the difference is found to be:

$$f_d' - f_d = -f_u \frac{\Delta C_x}{2(C + \Delta C_s)} + f_l \frac{\Delta C_x}{2C}. \tag{19}$$

i.e., not exactly null if $\Delta C_x \neq 0$, but small (and identical to zero if $\Delta C_s = 0$).

C. Simulated Sensitivity in terms of Permittivity

It is apparent that the optimum position (i.e., the most sensitive region) where the SUTs must be loaded depends on the technology of implementation. In microstrip technology, as is well known, most of the electric field is concentrated in the substrate. Therefore, the SUTs should be located between the SIR and the ground plane, like filling a parallel-plate structure. Otherwise, the sensitivity will be decreased. Figure 9 shows a 2D cut of the electric field amplitude simulated with C*ST Microwave Studio*, confirming that most of the electric field confinement lies below the wide section of the SIR (i.e., the electric field is dominated by the capacitance effect of the resonator). Moreover, since the field is roughly uniformly distributed, the wide section behaves approximately like a parallel-plate capacitance.

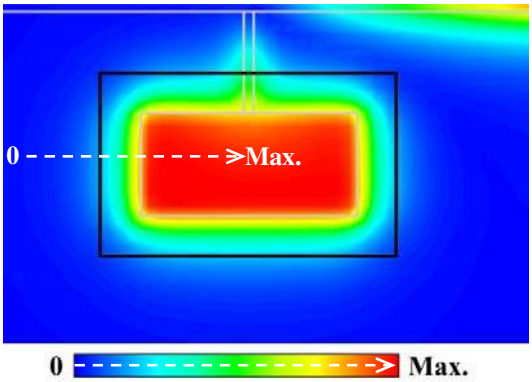

Fig. 9. Electric field amplitude at the SIR resonance frequency of the reference structure (single SIR) over the mid-plane between the SIR and the ground plane. The SUT height is set to $h-2t$ where $t = 35\ \mu$m, and its length and width extend 1 mm beyond the wide section of the SIR, as depicted. The SUT size is 4.6 mm x 7.5 mm x 812.8 μm.

In order to characterize the sensitivity in terms of permittivity perturbations, we have considered the same reference structures as in Section II [Figs. 3(a) and 5(a)], and we have introduced a bulk dielectric SUT in one of the SIRs as illustrated in Fig. 9. The structures have been simulated with different values of the SUT relative permittivity, ε_{r2}, and the resulting resonance frequencies are plotted in Fig. 10. The resulting sensitivity derived from the results in Fig. 10 is plotted in Fig. 11. Clearly, for small perturbations, the sensitivity in cascaded SIRs is superior to that obtained using parallel SIRs.

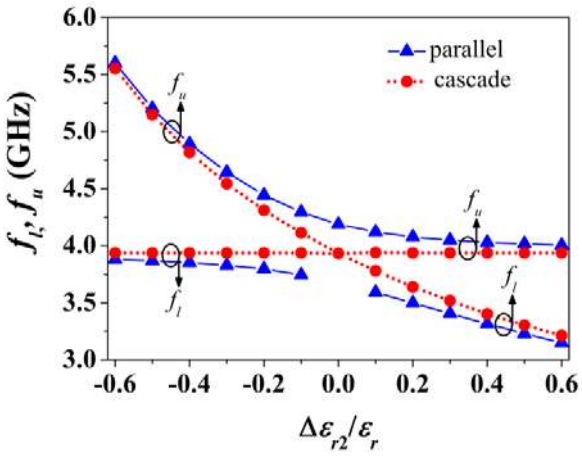

Fig. 10. Resonance frequencies for parallel and cascaded SIRs, obtained by electromagnetic simulation, versus a perturbation in the relative permittivity of a SUT loaded to one of the SIRs. The relative permittivity is perturbed by steps of ±10% so that $1.352 \le \varepsilon_{r2} \le 5.408$ ($-0.6 \le \Delta\varepsilon_{r2}/\varepsilon_r \le 0.6$) where $\varepsilon_r = 3.38$. Losses are considered.

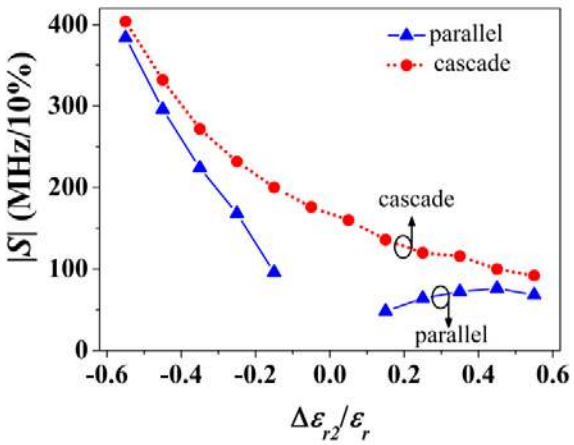

Fig.11. Magnitude of the sensitivity derived from Fig. 10 by steps of $\Delta\varepsilon_{r2}/\varepsilon_r = \pm 0.1$ (±10%). The sensitivity in the jump discontinuity of the parallel configuration is not calculated. As stated by (13), the sensitivity and the perturbation have the same sign.

It can be observed that the results in Fig. 10 are similar to those in Fig. 7. More specifically, the sensitivity to a permittivity perturbation ($\Delta\varepsilon_{r2}/\Delta\varepsilon_r$) is a bit smaller than that to a capacitive perturbation ($\Delta C_{s2}/\Delta C_s$) with the same amount of relative perturbation. This verifies again that the capacitance is not exactly proportional to the permittivity.

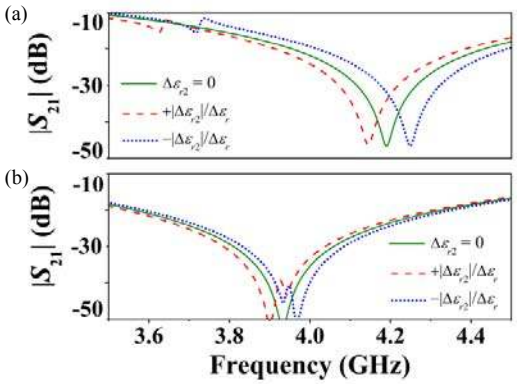

Fig. 12. Transmission coefficient obtained by electromagnetic simulations for small differential permittivity perturbations in (a) parallel and (b) cascaded SIRs. The perturbations are those necessary to obtain two −3-dB notches: $\Delta\varepsilon_{r2}/\varepsilon_r = \pm 0.06$ and ±0.02 (6% and 2%), respectively.

The discrimination for small differential inputs, ε_{rd}, is of relevant importance in comparators. To gain insight into the performance of the considered topologies to operate as comparators, the discrimination from balanced to unbalanced perturbations should be defined as the minimum ε_{rd} necessary to produce a discriminable doubly notched response. It is assumed that two −3-dB notches suffice for reasonable accurate discrimination. For the considered topologies, these values are about ±6% and ±2% in the parallel and cascaded configurations. The transmission coefficients for these inputs are plotted in Fig. 12. Therefore, the cascade configuration exhibits higher discrimination than the parallel one, and it is an appropriate means to enhance the capability of detecting

inputs as small as possible (i.e., to enhance the discrimination). As was expected, wideband notches are required. Otherwise losses may mask the notches, as occurs in the lower notch for parallel SIRs when the input differential permittivity is close to zero. In summary, the discrimination is better with the cascaded configuration, where both notches are wide.

On the other hand, in the case of large perturbations and as proven in Fig. 13, the parallel and cascaded configuration have similar resonance frequencies and, in turn, sensitivities.

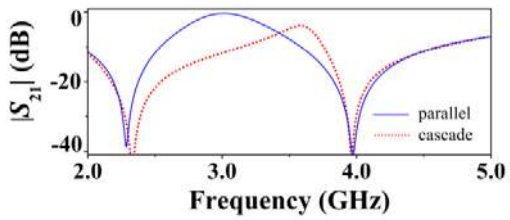

Fig. 13. Transmission coefficient obtained by electromagnetic simulations for a large differential permittivity perturbation: $\varepsilon_{r1} = 3.38$ and $\varepsilon_{r2} = 11.2$ resulting in $\Delta\varepsilon_{r2}/\varepsilon_r = +2.3$ (+230%).

IV. Experimental Validation of the Sensing Approaches and Discussion

In this section, permittivity perturbations are experimentally validated. To do so, the reference structures in Figs. 3 and 5 are considered again. In order to apply both positive and negative differential permittivity perturbations, the substrate in the vicinity of one of the SIRs is removed using a drilling machine, creating a cavity. Next, the cavity is either unfilled ($-|\Delta\varepsilon_{r2}|$) or filled with a *Rogers RO3010* substrate $\varepsilon_r = 11.2$ ($+|\Delta\varepsilon_{r2}|$), and covered with a metallic adhesive tape to act as the ground plane etched from the microstrip structure. Figure 14 shows different photographs to illustrate the cavities, and their filling and covering. Note that the effects of the air-gap present between the cavity and the SUT can be minimized by putting some pressure to the structure, as we have done in the measurements with the *Rogers* slab (in [5] a systematic method to eliminate the effects of the air gap is reported).

(a)

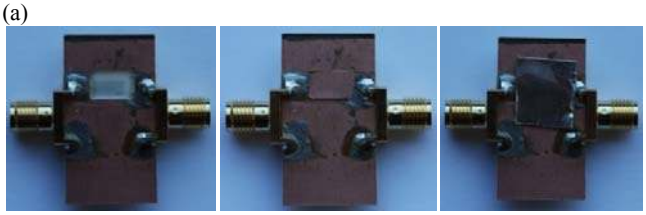

(b)

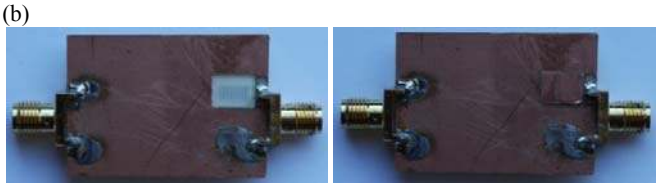

(c)

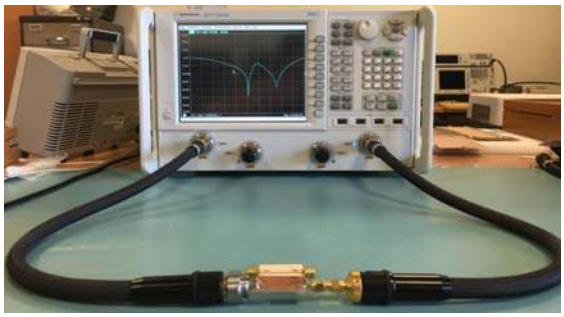

Fig. 14. Photograph of the reference structures composed of microstrip lines loaded with pairs of (a) parallel and (b) cascaded SIRs. From left to right: (*i*) cavity in one of the SIRs; (*ii*) filled cavity with *Rogers RO3010* with $\varepsilon_{r2} = 11.2$; (*iii*) cavity covered with a metallic tape. The photograph of the experimental set-up for measurement is shown in (c), including the *Agilent N5221* network analyzer, cables, connectors and sensing system.

(a)

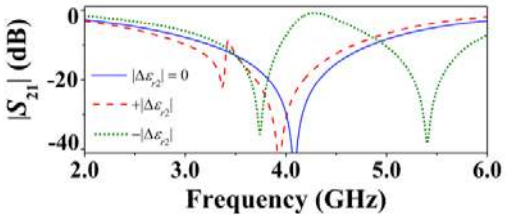

(b)

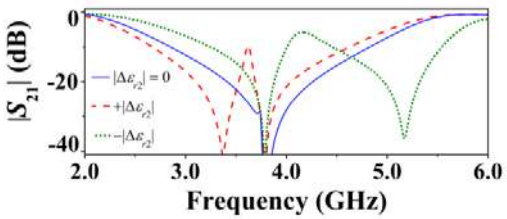

Fig. 15. Measured transmission coefficient magnitude for the (a) parallel and (b) cascaded topologies under dielectric loading. Three scenarios are considered: (*i*) without cavity ($\Delta\varepsilon_{r2} = 0$); (*ii*) unfilled cavity so that $\varepsilon_{r2} = 1$ ($-|\Delta\varepsilon_{r2}|$); (*iii*) filled cavity with *Rogers RO3010* with $\varepsilon_{r2} = 11.2$ ($+|\Delta\varepsilon_{r2}|$). No perturbation is applied to the other SIR ($\Delta\varepsilon_{r1} = 0$).

A. Determining the dielectric constant of the SUT

The measured results of the positive/negative perturbations, plotted in Fig. 15 together with those with no perturbation, are in accordance with theory. Even though the cavity dimensions cannot be controlled very accurately with the in-house drilling, these experiments validate the sensing principle under permittivity perturbation. Nevertheless, inspection of Fig. 15 reveals that the difference in notch frequencies is somehow smaller than the results of Fig. 10 for the considered dielectric constant values (1 for the unfilled cavity, and 11.2 for the filled cavity with the considered *Rogers* material). The reason

is that the cavity has been implemented by milling, and we have not completely removed all the substrate material, since the SIR needs some material for mechanical stability. Therefore, the unfilled cavity, including the remaining substrate layer, has an effective dielectric constant larger than 1, and the cavity filled with the *Rogers* substrate (dielectric constant 11.2) has actually an effective dielectric constant smaller than 11.2. In other words, the measurement provides the effective dielectric constant of the structure below the SIR, including not only the SUT but also the presence of a narrow dielectric layer of relative permittivity 3.38. Moreover, the thickness of the whole structure, layer on top the cavity plus SUT, is not necessarily the same as the thickness of the substrate. In the simulations that have been carried out to obtain the results of Fig. 10, we have not considered this substrate layer between the SIR metal level and the SUT. In practice, it is very difficult for us to precisely control the thickness of the remaining substrate between the SIR patch and the cavity. For this main reason such layer has not been considered in the simulations. However, note that with a more sophisticated fabrication technology (e.g., micromachining), such control would not be a problem.

Nevertheless, we have proposed a method to determine this thickness that subsequently allows us to obtain the dielectric constant of the SUT once the reference permittivity (the one of the substrate, i.e., ε_{r1}) and the thickness of the SUT are known. Let us consider that h_1 and h_c are the thicknesses of the substrate layer on top of the cavity and cavity, respectively, so that $h_1 + h_c = h$, the substrate thickness. Moreover let us assume that the SUT corresponds to a material with well-known dielectric constant, ε_{r2}, and thickness, h_2 (see Fig. 16). The method is based on the fact that the effective dielectric constant of the composite formed by the substrate layer on top of the cavity plus the SUT, ε_{eff}, is related to the respective dielectric constants by

$$\frac{\varepsilon_{eff}}{h} = \frac{\frac{\varepsilon_{r1}}{h_1}\cdot\frac{\varepsilon_{r2}}{h_2}}{\frac{\varepsilon_{r1}}{h_1}+\frac{\varepsilon_{r2}}{h_2}}. \tag{20}$$

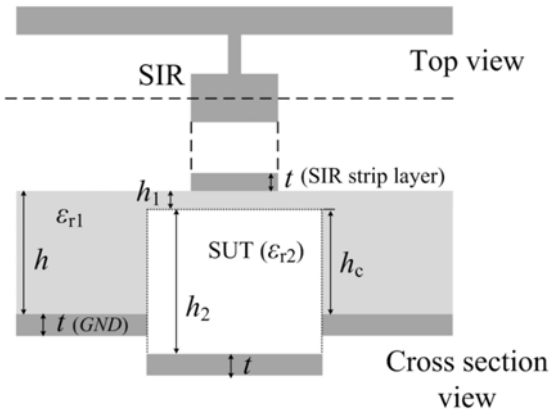

Fig. 16. Sketch (not drawn to scale) of the top and cross sectional view of the SIR and cavity loaded with the SUT.

From the previous expression, the dielectric constant of the SUT can be isolated:

$$\varepsilon_{r2} = \frac{\varepsilon_{eff}\varepsilon_{r1}h_2}{\varepsilon_{r1}h - \varepsilon_{eff}h_1}, \tag{21}$$

ε_{eff} can be inferred from the split in frequency of the SUT and the curve of Fig. 10 corresponding to the cascade connection. Thus, if ε_{r2} and h_2 are known, h_1 can be obtained from (21). For the SUT corresponding to the *Rogers* substrate with ε_{r2} = 11.2 and h_2 = 635 μm, and taking into account that the notch frequencies of Fig. 15(b) provide ε_{eff} = 4.9, according to Fig. 10, the resulting thickness of the layer on top of the cavity is found to be h_1 = 369 μm. To verify the validity of this result, we have considered the curve of Fig. 15(b) corresponding to the unfilled cavity (ε_{r2} = 1). By introducing the corresponding effective dielectric constant ε_{eff} = 1.69 in (21), and h_1 = 369 μm, the air thickness is found to be h_2 = 371 μm, which is in reasonable agreement with the thickness of the cavity (note however that the metallic tape is somehow flexible and hence may reduce the effective value of the cavity thickness).

Once h_1 is known, we have calculated the dielectric constant of another SUT, an *Arlon* slab with ε_{r2} = 2.43 and h_2 = 490 μm. The measured transmission coefficient for the cascaded configuration is depicted in Fig. 17. The effective dielectric constant that results from Fig. 10 is ε_{eff} = 2.70, and using (21), the dielectric permittivity is found to be ε_{r2} = 2.50, very close to the nominal value (2.43).

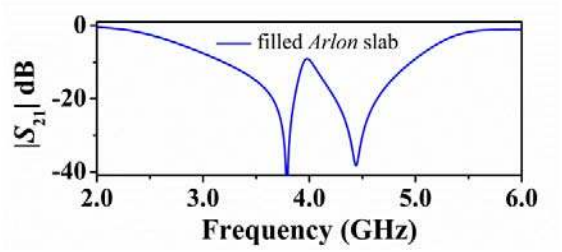

Fig. 17. Measured transmission coefficient magnitude for the cascaded topology with the cavity filled by an *Arlon* substrate with characteristics indicated in the text.

It is interesting to analyze expression (21), and the dependence of the dielectric constant of the SUT with the different parameters. Particularly, it depends linearly on the thickness of the SUT, h_2. Therefore, uncertainties in this parameter are directly translated to the dielectric constant. The dependence with the other geometrical parameters, h and h_1, can be appreciated in expression (21) as well. The thickness of the substrate, h, is typically known with good accuracy. On the other hand, the dependence on h_1 is modulated by ε_{eff}, and the effects of the uncertainty with this parameter are minimized in samples with small dielectric constant (and hence small ε_{eff}). In view of (21), and taking into account that ε_{eff} is roughly proportional to ε_{r1}, namely,

$$\varepsilon_{eff} = \varepsilon_{r1} + \Delta\varepsilon_{r2} = \varepsilon_{r1} + \frac{\Delta f}{S} \approx \varepsilon_{r1} + 2\varepsilon_{r1}\frac{\Delta f}{f_0}, \tag{22}$$

it follows that ε_{r2} is proportional to ε_{r1} (see 21) and hence the uncertainties in the dielectric constant of the reference material are (roughly) directly translated to the one of the measured material.

Comparison of the proposed differential sensor with other permittivity sensors based on microstrip technology, such as those sensors based on CSRRs [3]-[5] is not easy. Nevertheless, the fact that the proposed sensors are differential represents advantages in several aspects. As comparators, common-mode stimuli are minimized by means of a differential-mode approach, as discussed before, and small changes between two (apparently identical) samples can be detected. Comparators based on this approach can be of interest to determine defects or abnormalities in a sample, as compared to a well known reference, as well as soft permittivity changes in circuits manufactured on microwave laminates. In a real scenario, two identical cavities must be present, each one below the corresponding SIR patch.

Concerning sensitivity, the capacitance of the SIR is broadside and hence very sensitive to the permittivity, as compared to the case of edge capacitances (such as the one of CSRRs). The sensitivity that can be inferred from the sensors reported in [3]-[5] is very reasonable but not as good as the one reported here [of the order of 0.6 GHz for small perturbations, according to Fig. 10 and expression (13) –note that we have considered the relative permittivity, i.e., dimensionless, in the denominator of (13)]. Note that according to expression (13), such sensitivity can be modulated by means of the SIR dimensions, which provide the resonance frequency for the unperturbed state.

B. Loss tangent estimation

Even though this paper is focused on low-loss substrates and SUTs (as mentioned before), let us discuss a procedure to estimate the loss tangent. It is based on the depth of the notch (similar to [4],[5]), and for this reason a structure with a single SIR is preferred (i.e., non differential). Otherwise, the presence of closed notches (as results in cases with small differential permittivities) may obscure the results. The initial assumption is that the substrate material below the SIRs is completely removed and replaced with the SUT. Let us consider two causes of losses, i.e., metallic losses, mainly associated to the narrow inductive strip of the SIR, and dielectric losses, related to the SUT. The model of the SIR-loaded line with losses included is the one of Fig. 1(b), but including a resistance, R_M, in series with the inductance L_s, plus a resistance, R_D, parallel connected to the capacitance C_s. The impedance of this shunt branch is

$$Z_{in} = R_M + \frac{R_D}{1+R_D^2 C_s^2 \omega^2} + j\left(\omega L_s - \frac{R_D^2 C_s \omega}{1+R_D^2 C_s^2 \omega^2}\right), \quad (23)$$

and this expression can be approximated by

$$Z_{in} = R_M + \frac{1}{R_D C_s^2 \omega^2} + j\left(\omega L_s - \frac{1}{C_s \omega}\right), \quad (24)$$

where it has been assumed that $R_D^2 C_s^2 \omega^2 >> 1$, corresponding to SUTs with moderate or low-loss levels (note that in an ideal lossless SUT, $R_D = \infty$). At the notch frequency, the reactive part of Z_{in} nulls, and the resulting resistance can be expressed as

$$R_{LOSS} = R_M + \frac{1}{C_s \omega Q_D}, \quad (25)$$

where Q_D is the SUT quality factor. Such resistance is related to the magnitude of the transmission coefficient at the notch frequency by

$$R_{LOSS} = \frac{Z_0 |S_{21}|}{2(1-|S_{21}|)}, \quad (26)$$

and therefore it can be inferred from the measured frequency response. On the other hand,

$$\tan\delta = \frac{1}{R_D C_s \omega} = Q_D^{-1}. \quad (27)$$

If R_M is known, (25) gives Q_D and hence $\tan\delta$ can be inferred from (27). To determine the contribution of the metallic losses, R_M, a possible procedure is to consider a reference SUT (or substrate) with a well-known $\tan\delta$ (and hence Q_D). From (25), R_M can be isolated, and used subsequently for the determination of the loss tangent of the SUT (it is assumed that R_M does not vary with the SUT).

The previous procedure cannot be directly applied in general to our proof-of-concept cascaded SIR based sensor since it is based on two SIRs, and, moreover, there is a remaining substrate layer on top of the cavity. However, for the considered SUT, the *Arlon* slab with nominal permittivity and thickness ε_{r2} = 2.43 and h_2 = 490 μm, the frequency response shows quite uncoupled notches and, therefore, we can modify the procedure and at least make an estimation of the $\tan\delta$. By introducing the SUT into the cavity, expression (25) can be re-written as

$$R_{LOSS} = R_M + \frac{1}{C_1 \omega Q_1} + \frac{1}{C_2 \omega Q_2}, \quad (28)$$

where the sub-index 1 and 2 refer to the layer on top of the cavity and SUT, respectively. By identifying the last two terms with the loss contribution of the composite, $(C_{eq}\omega Q_{eq})^{-1}$, it follows that

$$Q_{eq} = \frac{(C_1 + C_2) Q_1 Q_2}{Q_1 C_1 + Q_2 C_2}. \quad (29)$$

This expression depends on the ratio C_2/C_1, which can be determined from the thickness of the layer and SUT and from the dielectric constants. Using (25) with $C_s = C_{eq}$ and $Q_D = Q_{eq}$ and with R_{LOSS} inferred from (26), where S_{21} is obtained from the depth of the second notch in Fig. 17, we can determine Q_{eq}, which is found to be Q_{eq} = 366. Since Q_1 is known ($Q_1 = \tan\delta)^{-1}$ = 476, we can isolate Q_2 from (29), and the resulting

value is found to be Q_2 = 353, which gives tanδ = 0.0028 (in reasonable agreement with the nominal value of 0.0020). Note that we cannot expect an accurate value of the loss factor with the considered in-house measurement system, necessarily affected by additional losses such as those derived from the connectors, soldering, metallic adhesive tape, etc. Nevertheless, a procedure to estimate the tanδ of the SUT has been reported.

V. Conclusions

This paper analyzes two simple strategies to conduct differential measurements of permittivity. These strategies are based on loading pairs of stepped impedance resonators (SIRs), in either parallel or cascade connection, to a microstrip line. It has been shown that, although the most canonical symmetric configuration to perform a differential measurement is the one where the SIRs are parallel-connected, such a structure exhibits lower performance for small differential permittivities due to inter-resonator coupling, and hence the cascade connection is preferred in these situations. The differential technique is simple, as a transmission line is driven with a single-ended RF/microwave signal, and the SIRs are simply simultaneously and individually loaded with dielectric materials. The sensing principle is based on resonance frequency splitting, so that when the permittivities of the two dielectric materials are identical the sensor exhibits a single resonance frequency, whereas two resonances are present if such permittivities are different. The sensing principle has been experimentally validated by both shape and material perturbations. This main focus in this work has been on the differential measurement. A method to determine the dielectric constant of a certain sample under test (SUT), provided the one of the reference is known, has been proposed. Finally, in spite that the analysis of the present work has been carried out by excluding losses, a method to estimate the loss tangent of the SUT has been also reported. As is well known, changing environmental factors may change the permittivity and, therefore, miscalibrate. By virtue of a differential measurement, sensing and comparison with some degree of immunity to these external factors is expected.

References

[1] E. Nyfor, "Industrial microwave sensors—A review," *Subsurface Sensing Technologies and Applications*, vol. 1, no. 1, pp. 23−43, Jan. 2000.

[2] M. Tiuri, "Microwave Sensor Applications in Industry," in *Europ. Microw. Conf.*, pp. 25−32, Sep. 1987.

[3] M. S. Boybay and O. M. Ramahi, "Material characterization using complementary split-ring resonators," *IEEE Trans. Instrum. Meas*., vol. 61, no. 11, pp. 3039−3046, Nov. 2012.

[4] C.-S. Lee and C.-L. Yang, "Complementary split-ring resonators for measuring dielectric constants and loss tangents," *IEEE Microw. Wireless Compon. Lett.*, vol. 24, no. 8, pp. 563−565, Aug. 2014.

[5] C.-L. Yang, C.-S. Lee, K.-W. Chen, and K.-Z. Chen, "Noncontact measurement of complex permittivity and thickness by using planar resonators," *IEEE Trans. Microw. Theory Techn.*, vol. 64, no.1, pp. 247−257, Jan. 2016.

[6] M. Puentes, C. Weiß, M. Schüßler, and R. Jakoby, "Sensor array based on split ring resonators for analysis of organic tissues," in *IEEE MTT-S Int. Microw. Symp.*, Baltimore, MD, USA, pp. 1-4, Jun. 2011

[7] M. Puentes, *Planar Metamaterial Based Microwave Sensor Arrays for Biomedical Analysis and Treatment*. Springer, 2014.

[8] T. Chretiennot, D. Dubuc and K. Grenier, "A microwave and microfluidic planar resonator for efficient and accurate complex permittivity characterization of aqueous solutions," *IEEE Trans. Microw. Theory Techn.*, vol. 61, no. 2, pp. 972−978, Feb. 2013.

[9] A. Abduljabar, D. Rowe, A. Porch and D. Barrow, "Novel microwave microfluidic sensor using a microstrip split-ring resonator," *IEEE Trans. Microw. Theory Techn*., vol. 62, no. 3, pp. 679−688, Mar. 2014.

[10] A. Ebrahimi, W. Withayachumnankul, S. Al-Sarawi and D. Abbott, "High-sensitivity metamaterial-inspired sensor for microfluidic dielectric characterization," *IEEE Sensors J.*, vol. 14, no. 5, pp. 1345−1351, May 2014.

[11] W. Withayachumnankul, K. Jaruwongrungsee, A. Tuantranont, C. Fumeaux and D. Abbott, "Metamaterial-based microfluidic sensor for dielectric characterization," *Sensor Actuat. A Phys.*, vol. 189, pp. 233−237, Jan. 2013

[12] H.-J. Lee and J.-G. Yook, "Biosensing using split-ring resonators at microwave regime," *App. Phys. Lett*., vol. 92, no. 25, paper 254103, 2008.

[13] K. Grenier, D. Dubuc, P-E. Poleni, M. Kumemura, H. Toshiyoshi, T. Fujii, and H. Fujita, "Integrated broadband microwave and microfluidic sensor dedicated to bioengineering," *IEEE Trans. Microw. Theory Techn*., vol. 57, no. 12, pp. 3246−3253, Dec. 2009.

[14] T. Chen, D. Dubuc, and K. Grenier, "Resonant-based microwave biosensor for physiological liquid identification", *Europ. Microw. Conf*, pp. 448-450, Amsterdam, Netherland, Oct-Nov, 2012.

[15] T. Chretiennot, D. Dubuc, K. Grenier, "Optimized Electromagnetic Interaction Microwave Resonator/Microfluidic Channel for Enhanced Liquid Bio-Sensor," *Europ. Microw. Conf.*, pp. 464-467, Nuremberg Germany, Oct.2013.

[16] T. Chretiennot, D. Dubuc, K. Grenier, "Double stub resonant biosensor for glucose concentrations quantification of multiple aqueous solutions," *IEEE MTT-S Int. Microw. Symp*., pp. 1-4, Tampa (FL), June 2014.

[17] E. Ekmekci and G. Turhan-Sayan, "Multi-functional metamaterial sensor based on a broad-side coupled SRR topology with a multi-layer substrate," *App. Phys. A* , vol. 110, no. 1, pp 189−197, Jan. 2013.

[18] C. Damm, M. Schussler, M. Puentes, H. Maune, M. Maasch and R. Jakoby, "Artificial transmission lines for high sensitive microwave sensors," *IEEE Sensors Conf.,* Christchurch, New Zealand, pp.755−758, Oct. 2009.

[19] C. Damm, *Artificial Transmission Line Structures for Tunable Microwave Components and Microwave Sensors*, Shaker, 2011.

[20] M. Schueler, C. Mandel, M. Puentes and R. Jakoby, "Metamaterial inspired microwave sensors," *IEEE Microw. Mag.*, vol. 13, no. 2, pp. 57–68, Mar. 2012.

[21] J. G. Webster, *The Measurement Instrumentation and Sensors Handbook*. Boca Raton, FL, USA: CRC, 1999.

[22] J. Fraden, *Handbook of Modern Sensors: Physics, Design, and Applications*, 3rd ed. New York, NY, USA, Springer, 2004.

[23] J. Naqui, C. Damm, A. Wiens, R. Jakoby, L. Su and F. Martín, "Transmission lines loaded with pairs of magnetically coupled stepped impedance resonators: modeling and application to microwave sensors," in *IEEE MTT-S Int. Microw. Symp*., Tampa, FL, USA, pp. 1-4, Jun. 2014.

[24] J. Naqui, *Symmetry properties in transmission lines loaded with electrically small resonators: circuit modeling and applications*, Springer, 2016.

[25] A.K. Horestani, J. Naqui, Z. Shaterian, D. Abbott, C. Fumeaux and F. Martín, "Two-dimensional alignment and displacement sensor based on movable broadside-coupled split ring resonators," *Sens. Actuat. A Phys*., vol. 210, pp. 18–24, Apr. 2014.

[26] J.-S. Hong and M. J. Lancaster, *Microstrip Filters for RF/Microwave Applications*. New York, NY, USA: Wiley, 2001.

[27] J. Bonache, M. Gil, I. Gil, J. García-García and F. Martín, "On the electrical characteristics of complementary metamaterial resonators," *IEEE Microw. Wireless Compon. Lett.,* vol. 16, no. 10, pp. 543−545, Oct. 2006.

[28] R. Mongia, I. Bahl and P. Barthia, *RF and Microwave Coupled Line Circuits*. Norwood, MA, USA: Artech House, 1999.

[29] C. Cui and Y. Liu, "Quad-band bandpass filter design by embedding dual-band bandpass filter with dual-mode notch elements," *Electron. Lett.*, vol. 50, no. 23, pp.1719–1720, Nov. 2014.

[30] M. Makimoto and S. Yamashita, "Compact bandpass filters using stepped impedance resonators," *Proc. IEEE*, vol. 67, no. pp. 16−19, Jan. 1979.

[31] D. Girbau, A. Lazaro and R. Villarino, "Passive wireless permittivity sensor based on frequency-coded chipless RFID tags," in *IEEE MTT-S Int. Microw. Symp*., Montreal, Canada, pp. 1-4, Jun. 2012.

[32] J.-S. Hong, H. Shaman and C. Young-Hoon, "Dual-mode microstrip open-loop resonators and filters," *IEEE Trans. Microw. Theory Techn*., vol. 55, no. 8, pp. 1764−1770, Aug. 2007.

[33] V. A. Fedotov, M. Rose, S. L. Prosvirnin, N. Papasimakis and N. I. Zheludev, "Sharp trapped-mode resonances in planar metamaterials with a broken structural symmetry," *Phys. Rev. Lett*, vol. 99, no. 14, paper 47401, Oct. 2007.